J. Fluid Mech. (1996), *vol.* 313, *pp.* 105–130

Experimental and numerical study of the interaction between a planar shock wave and a square cavity

By O. IGRA[1], J. FALCOVITZ[2], H. REICHENBACH[3] AND W. HEILIG[3]

[1] Pearlstone Center for Aeronautical Engineering Studies, Department of Mechanical Engineering, Ben-Gurion University of the Negev, Beer Sheva, Israel

[2] Faculty of Aerospace Engineering, Israel Institute of Technology, Haifa, Israel

[3] Ernst Mach Institute, Freiburg, Germany

(Received 6 February 1995 and in revised form 30 June 1995)

The interaction of a planar shock wave with a square cavity is studied experimentally and numerically. It is shown that such a complex, time-dependent, process can be modelled in a relatively simple manner. The proposed physical model is the Euler equations which are solved numerically, using the second-order-accurate high-resolution GRP scheme, resulting in very good agreement with experimentally obtained findings. Specifically, the wave pattern is numerically simulated throughout the entire interaction process. Excellent agreement is found between the experimentally obtained shadowgraphs and numerical simulations of the various flow discontinuities inside and around the cavity at all times. As could be expected, it is confirmed that the highest pressure acts on the cavity wall which experiences a head-on collision with the incident shock wave while the lowest pressures are encountered on the wall along which the incident shock wave diffracts. The proposed physical model and the numerical simulation used in the present work can be employed in solving shock wave interactions with other complex boundaries.

1. Introduction

The interaction of shock waves with rigid boundaries has been the subject of many investigations during the past four decades. They were motivated by the fact that shock wave diffractions arise in a variety of important applications. A commonplace technological application is an internal combustion engine, where inflow/outflow valves are periodically opened and shut giving rise to complex shock and rarefaction wave patterns. Another type of important application is in the area of public safety: the vulnerability of buildings to air blasts generated by either a bomb explosion or an industrial accident. As is well known, a blast effect is transmitted to fairly large distances via wave propagation, so that structure loading histories are governed by complex shock wave diffraction/reflection phenomena. Owing to the complexity of such interactions, investigations performed in the 1950s and the 1960s were limited to experimental studies conducted in supersonic wind tunnels and/or shock tubes. With the advent of fast computers and the development of accurate and efficient numerical schemes, attempts were made to numerically solve the flow fields arising in such interactions. Naturally, past investigations centred on relatively simple configurations. For example, shock wave reflection from wedges of various geometries received much

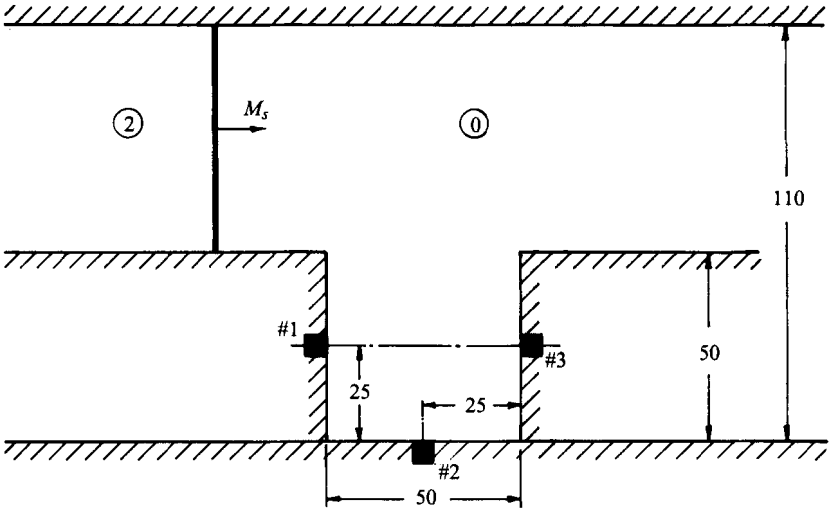

FIGURE 1. Schematic description of the flow field considered prior to the arrival of the incident shock wave at the cavity. All dimensions are in mm. Solid squares show pressure transducers, labelled nos 1–3. The computation domain is a rectangle 210 × 110 mm, starting 50 mm to the left of the cavity.

attention and by now are well known and documented, e.g. see Ben-Dor (1991). Notably wedge interactions result in a pseudo-steady (self-similar) flow having a similar wave pattern throughout the interaction processes.

The purpose of the present study is to analyse a complex shock wave interaction with rigid boundaries, an interaction which is truly non-stationary and possesses no similarity throughout its duration. An example of such a flow is the case of a planar shock wave propagation over a flat surface in which a square cavity is embedded; see figure 1. The interaction of the planar shock wave with such a cavity is studied both experimentally and numerically. As will be shown, such interaction is truly non-stationary and no similarity pattern can be identified in this flow field. It is noted that a few attempts were made in the recent past to study such flows, for example Gvozdeva *et al.* (1988) and Bazhenova *et al.* (1990). In these investigations the flow field was studied experimentally, using toepler and interferometric flow visualization techniques. In addition, an attempt was made to predict the post-shock flow pressure using the two-dimensional Whitham approximation. As will be shown subsequently the experimental as well as the theoretical studies of these papers failed to cover experimentally, and to reproduce theoretically, the investigated flow field. The proposed numerical scheme GRP (Generalized Riemann Problem) replicates the experimentally observed wave patterns (shock and contact discontinuities) quite accurately. Measured maxima of pressure time-histories on cavity walls were also reproduced by the computations. The present investigation thus offers a complete experimental coverage of the considered interaction process and a comprehensive numerical simulation which is shown to be in good agreement with the experimental findings.

The plan of this paper is to introduce the theoretical modelling (Euler equations) in §2, followed by an outline of the numerical scheme GRP in §3. The results of experiments and computations are presented and compared in §4. The study is summarized in §5.

2. Theoretical background

The flow field which results from the interaction of a normal shock wave with a square cavity, as shown in figure 1, is a two-dimensional, non-stationary flow. Assuming that the fluid is inviscid and non-conductive, the governing equations (expressing conservation of mass, momentum and energy) can be written as follows:

conservation of mass

$$\frac{\partial \rho}{\partial t}+\frac{\partial}{\partial x}(\rho u)+\frac{\partial}{\partial y}(\rho v)=0; \tag{1}$$

conservation of x-momentum,

$$\frac{\partial}{\partial t}(\rho u)+\frac{\partial}{\partial x}(\rho u^2+p)+\frac{\partial}{\partial y}(\rho uv)=0; \tag{2}$$

conservation of y-momentum,

$$\frac{\partial}{\partial t}(\rho v)+\frac{\partial}{\partial x}(\rho uv)+\frac{\partial}{\partial y}(\rho v^2+p)=0; \tag{3}$$

conservation of energy,

$$\frac{\partial}{\partial t}(\rho E)+\frac{\partial}{\partial x}[u(\rho E+p)]+\frac{\partial}{\partial y}[v(\rho E+p)]=0; \tag{4}$$

where ρ, u, v, p and E are the density, the x-component and the y-component of the flow velocity vector, pressure and specific total energy, respectively; x, y and t, the independent variables, are Cartesian coordinates and time, respectively. The system of equations (1)–(4) contains five dependent variables (ρ, u, v, p and E). For its solution an additional equation, the equation of state, is needed. For a perfect gas the equation of state is

$$\left.\begin{aligned} p &= (\gamma-1)\rho e, \\ e &= E-(u^2+v^2)/2, \end{aligned}\right\} \tag{5}$$

where e stands for the flow internal energy per unit mass and γ is the ratio of specific heats.

The assumption that the fluid is an inviscid and non-conductive perfect gas is quite reasonable for the flow considered for the following reasons. As long as the incident shock wave Mach number is moderate, i.e. $M_s < 4$, the post-shock gas temperature is not too high (less than 1200 K for a diatomic gas and for $T_0 = 300$ K). Therefore, real gas effects can be ignored and the gas behaves virtually as a perfect gas. In subsequent solutions of (1)–(5) the highest incident shock wave Mach number is $M_s = 2.032$; for such a case the ideal gas assumption is amply justified. The assumption of an inviscid and non-conductive gas is also reasonable since for the relatively short flow duration the amount of heat transfer and viscous effects, in and around the square cavity, are negligibly small in comparison with the flow specific energy and momentum, and can therefore be ignored. The validity of these assumptions is supported by the good agreement between the numerical results obtained by solving numerically (1)–(5) and the experimental findings, as will be presented below.

Equations (1)–(4) are nonlinear partial differential equations. An analytical solution to these equations is not available. Therefore, one is compelled to resort to numerical methods. The numerical scheme used for the solution of (1)–(5) is the GRP (Generalized Riemann Problem). This scheme is of a second-order accuracy and is especially suitable for producing solutions to compressible flows with shock or contact discontinuities. Details regarding the formulation of the GRP scheme are available in Ben-Artzi & Falcovitz (1984, 1986) and in Falcovitz & Ben-Artzi (1995). This scheme is formulated for flows in one space dimension. In the following, we present a brief description of the GRP scheme and its extension to two space dimensions via operator splitting.

3. Numerical scheme

The Euler equations (1)–(4) expressing the conservation of mass, momentum and energy are now concisely written as

$$\frac{\partial}{\partial t}U+\frac{\partial}{\partial x}F(U)+\frac{\partial}{\partial y}G(U)=0, \tag{6a}$$

$$U(x,y,t)=\begin{bmatrix}\rho\\ \rho u\\ \rho v\\ \rho E\end{bmatrix};\quad F(U)=\begin{bmatrix}\rho u\\ \rho u^2+p\\ \rho uv\\ (\rho E+p)u\end{bmatrix};\quad G(U)=\begin{bmatrix}\rho v\\ \rho uv\\ \rho v^2+p\\ (\rho E+p)v\end{bmatrix}. \tag{6b}$$

The two-dimensional finite-difference scheme for the integration of (6) is constructed from the one-dimensional GRP conservation law scheme (Ben-Artzi & Falcovitz 1984, 1986; Falcovitz & Ben-Artzi 1995) via the well-known operator-splitting procedure proposed by Strang (1968). The splitting consists in replacing the system (6*a*) by the following pair of one-dimensional conservation laws:

$$\frac{\partial}{\partial t}U+\frac{\partial}{\partial x}F(U)=0,\quad \frac{\partial}{\partial t}U+\frac{\partial}{\partial y}G(U)=0, \tag{7a, b}$$

where system (7) is taken to mean that an integration by an infinitesimal time step dt of (6*a*) is obtained if an integration of U by dt according to (7*a*) is followed by a dt integration of U in (7*b*). Assume that a one-dimensional second-order-accurate finite-difference scheme is available and denote its integration operator for time step Δt by $L_x(\Delta t)$, $L_y(\Delta t)$ corresponding to (7*a*) and (7*b*), respectively. It was shown by Strang (1968) that the operator $L(\Delta t)$ given by

$$L(\Delta t)=L_x(\Delta t/2)\,L_y(\Delta t)\,L_x(\Delta t/2) \tag{8}$$

is a second-order finite-difference approximation to (6*a*).

Observe that in a sequence of numerous finite-difference integration steps $L(\Delta t)\,L(\Delta t)\ldots L(\Delta t)$, the half-step pairs of $L_x(\Delta t/2)$ operators can be combined into a single $L_x(\Delta t)$ operator to within second-order accuracy. This observation leads to the simplified splitting

$$L(\Delta t)=L_x(\Delta t)\,L_y(\Delta t) \tag{9}$$

instead of the more accurate and less efficient splitting given in (8). Computations of shock wave diffractions in the present study, as well as in other studies of shock wave phenomena, yield virtually indistinguishable results when using (8) or (9). We thus generally opt for the more efficient splitting, i.e. (9).

We now turn to the one-dimensional GRP scheme for (7*a*), which is formulated as follows. Let the computational domain be divided into a grid of equally spaced points $x_{i+1/2} = (i+1/2)\Delta x$, where Δx is the grid spacing and the ith cell is the interval $x_{i-1/2} < x < x_{i+1/2}$. The conservative second-order difference scheme for the time integration of the conservation laws, (7*a*), is

$$\left.\begin{aligned} U_i^{n+1} &= U_i^n - \frac{\Delta t}{\Delta x}[F(U)_{i+1/2}^{n+1/2} - F(U)_{i-1/2}^{n+1/2}], \\ \Delta t &= t^{n+1} - t^n, \end{aligned}\right\} \tag{10}$$

where U_i^n denotes the average value of U in cell i at time $t = t_n = n\Delta t$, and where the time-centred fluxes $F(U)_{i+1/2}^{n+1/2}$ are obtained by starting from linear distributions of flow variables in cells as proposed by van Leer (1979), and by employing the following analytic procedure. Denote by $U_i^n(x)$ the linear distribution of flow variables in cell i at time $t = n\Delta t$, whose average value is $U_i^n = U_i^n(x_i)$. Consider the initial value problem which constitutes an extension to the Riemann problem, and is named a Generalized Riemann Problem (GRP),

$$\frac{\partial}{\partial t}U + \frac{\partial}{\partial x}F(U) = 0, \tag{11a}$$

$$U(x, t_n) = \begin{cases} U_i^n(x), & x < x_{i+1/2} \\ U_{i+1}^n(x), & x > x_{i+1/2}. \end{cases} \tag{11b}$$

The key assumption of the GRP analysis is that as $t - t_n \to 0^+$ the solution $U(x,t)$ to (11) approaches smoothly the solution of the 'associated' Riemann problem defined in the following manner. Replace the linear distributions in (11*b*) by the constant distributions $U_i^n(x_{i+1/2})$, $U_{i+1}^n(x_{i+1/2})$, and consider the ensuing Riemann problem. Denote its self-similar solution by $U_{RP}[(x-x_{i+1/2})/(t-t_n)]$. Then the solution to (11) is assumed to have the property

$$\lim_{t-t_n \to 0^+} U(x_{i+1/2}, t) = U_{RP}(0). \tag{12}$$

Using this limit as the value of $U_{i+1/2}^n$, the flux at the mid-step is given by

$$F(U)_{i+1/2}^{n+1/2} = F(U)_{i+1/2}^n + \frac{\Delta t}{2}\left[\frac{\partial}{\partial t}F(U)\right]_{i+1/2}^n + O(\Delta t^2), \tag{13a}$$

$$\left[\frac{\partial}{\partial t}F(U)\right]_{i+1/2}^n = F'(U_{i+1/2}^n)\left[\frac{\partial}{\partial t}U\right]_{i+1/2}^n, \tag{13b}$$

where $F'(U)$ denotes the Jacobian matrix of $F(U)$ with respect to U. The evaluation of the time derivative in (13*b*) is the analytic core of the GRP method. The reader is referred to Ben-Artzi & Falcovitz (1984, 1986) and to Falcovitz & Ben-Artzi (1995) for a detailed presentation.

Two options are available for the analytic evaluation of $F(U)_{i+1/2}^{n+1/2}$. The exact GRP method, denoted E_∞, is based on an exact expression for the time derivative $[(\partial/\partial t)\,U]_{i+1/2}^n$ in (13*b*). The approximate E_1 scheme is based on the observation that an error of $O(\Delta t)$ in $[(\partial/\partial t)\,U]_{i+1/2}^n$ implies an error of $O(\Delta t^2)$ in the time-centred flux of (13*b*), i.e. the order of accuracy of the E_1 scheme is the same as that of the E_∞ scheme.

The E_1 scheme is obtained when (11 *a*) is replaced by a linearized conservation law (i.e. the so-called acoustic approximation).

Following the integration of the conservation laws, the one-dimensional scheme requires an updating of slopes of flow variables in cells, subjected to monotonicity constraints designed to avoid erroneous interpolations through hydrodynamic jumps (such as shocks or contact discontinuities). The van Leer (1979) monotonicity scheme was imposed on slopes of primitive variables (u, v, ρ, p in the two-dimensional case).

Turning now to the two-dimensional flow described by (6 *a*), the only modifications to the truly one-dimensional GRP scheme are the inclusion of the transverse velocity components in the kinetic energy expression, and the addition of a transverse momentum. The GRP analysis and scheme for one-dimensional flows are described in detail in the previously cited references. Therefore, we shall concentrate in the following solely on the presentation of those aspects of the scheme that are specific to two-dimensional flows.

It is sufficient to consider the L_x operator, since the L_y operator can be derived by analogy. Turning to the conservation of the y-component of momentum, the flux term (ρuv) in the L_x operator is treated by the GRP scheme as pure advection since the accelerating y-component of the pressure gradient is absent from L_x. Physically speaking, this corresponds to the assumption that in the x-direction fluid particles advected through cell interfaces retain their transverse velocity component v throughout the time step Δt, regardless of any wave structure resolving the discontinuity at each cell interface at time $t-t^n = 0^+$. However, since the average gradient $\partial v/\partial \xi$ per cell is included in the GRP scheme (ξ is the local Lagrange coordinate defined as $\mathrm{d}\xi = \rho \mathrm{d}x$), the flux ρuv at the cell interface $x_{i+1/2}$ is not constant throughout the time step. To evaluate the flux and its first time derivative at cell interfaces we adopt the following notation. Let Q denote any flow variable, and let $Q(x, t)$ denote the solution to the GRP at the cell interface $x = x_{i+1/2}$. Then we denote by Q_x and $\dot{Q}_x$ the values of $Q(x, t)$ and $\partial Q(x, t)/\partial t$ at $x = x_{i+1/2}$ and at $t-t^n = 0^+$, respectively. Using this notation, the time derivative $\dot{v}_x$ of the advected transverse velocity component v_x is given by

$$\dot{v}_x = -\rho_x u_x \left(\frac{\partial v}{\partial \xi}\right), \tag{14}$$

where we reiterate the previously mentioned interpretation of (14) as meaning that v in the fluid advected through the cell interface depends solely on the local Lagrange variable ξ (i.e. v is constant in time for fixed ξ which corresponds to a fixed fluid particle).

The analytical evaluation of cell interface variables and their first time derivatives is the main outcome of the GRP analysis; for details see Ben-Artzi & Falcovitz (1984). Here we assume that these values have already been evaluated for all primitive variables, i.e. for u, v, ρ, p, and we proceed to specify the resulting expressions for flux components and their time derivatives. The flux components are given by

$$F(U)^n_{i+1/2} = \begin{bmatrix} \rho_x u_x \\ \rho_x u_x^2 + p_x \\ \rho_x u_x v_x \\ u_x \left[\dfrac{\gamma}{\gamma - 1} p_x + \tfrac{1}{2} \rho_x (u_x^2 + v_x^2) \right] \end{bmatrix}. \tag{15}$$

By taking the time derivative of the flux components given in (15), the following expression is obtained:

$$\left[\frac{\partial}{\partial t}F(U)\right]^{n}_{i+1/2} = \begin{bmatrix} \rho_x \dot{u}_x + \dot{\rho}_x u_x \\ 2\rho_x u_x \dot{u}_x + \dot{\rho}_x u_x^2 + \dot{p}_x \\ \rho_x u_x \dot{v}_x + \rho_x \dot{u}_x v_x + \dot{\rho}_x u_x v_x \\ \dot{u}_x\left[\frac{\gamma}{\gamma-1}p_x + \frac{1}{2}\rho_x(u_x^2+v_x^2)\right] \\ \quad + u_x\left[\frac{\gamma}{\gamma-1}\dot{p}_x + \frac{1}{2}\dot{\rho}_x(u_x^2+v_x^2) + \rho_x(u_x\dot{u}_x + v_x\dot{v}_x)\right] \end{bmatrix}, \tag{16}$$

where the time derivative of v_x is given by (14) and all other variables along with their time derivatives are evaluated from the analytic expressions resulting from the GRP analysis.

In executing the numerical solution the flow field shown in figure 1 was divided into a grid of 990×495 equal-size (square) cells. Such a division ensured high resolution in the numerical reconstruction of the investigated flow field. The E_1 scheme was applied to all cell–cell interfaces where the pressure jump in both right- and left-hand waves resolving the associate Riemann problem was lower than 1 % of the pressure ahead of the wave. The CPU time saving thus achieved was 30 %.

4. Results and discussion

The experimental part of the present work was conducted in the shock tube of the Ernst Mach Institute in Freiburg, Germany. This shock tube has an inner diameter of 20 cm. The driver section is 180 cm long, the driven section is 888 cm long and the test section is located about 721 cm downstream of the diaphragm. A schematic description of this shock tube is shown in figure 2. Cellulose acetate sheets were used as diaphragms for separating the two sections. This was proven to be an excellent diaphragm material since it is brittle when stretched and has a high breaking velocity. The shock tube has a test section equipped with planar, parallel windows of high optical quality glass. The optical field of view is 200 mm × 110 mm and its depth is 40 mm. It is designed for using 'two-dimensional' models. Three sets of experiments were conducted. In the first, the interaction of an incident shock wave, whose Mach number was 1.30, with a square cavity (shown in figure 1) was studied using high-speed shadowgraph photography. In the second, the incident shock wave Mach number was increased to 2.085. In each of these two sets of experiments shadowgraphs were taken at preset time intervals (20 μs for the first and 12.5 μs for the second) covering the entire experimental flow duration. Unlike Gvozdeva *et al.* (1988) and Bazhenova *et al.* (1990) results, the present shadowgraphs provide details of the passage of the incident shock wave over the cavity and the wave pattern which resulted from this interaction. The shadowgraphs were obtained using a 24 frame Cranz-Schardin Spark Camera. Twenty-four point spark sources are focused onto the 24 objectives of the camera by use of a concave mirror. At the instant of ignition a spark is projected onto the film through the object lenses into which the image of the spark was copied. The advantage of this photographic technique is that there are no movable parts in the light ray path. Therefore, the optical resolution is determined only by the aperture of the objectives. In the third set of experiments pressure measurements were made (using Kistler 606 pressure transducers)

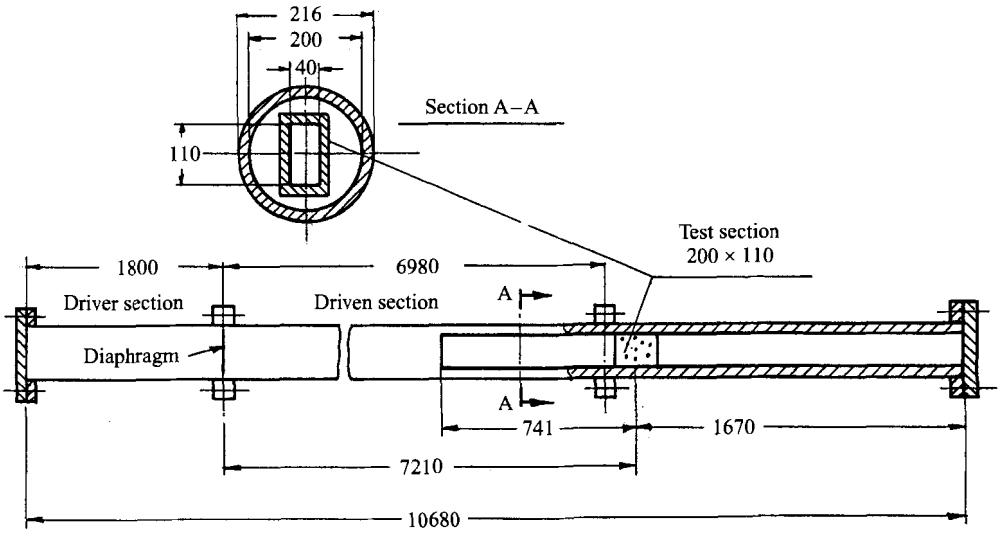

FIGURE 2. Illustration of the shock tube used for the experimental investigations. Dimensions in mm.

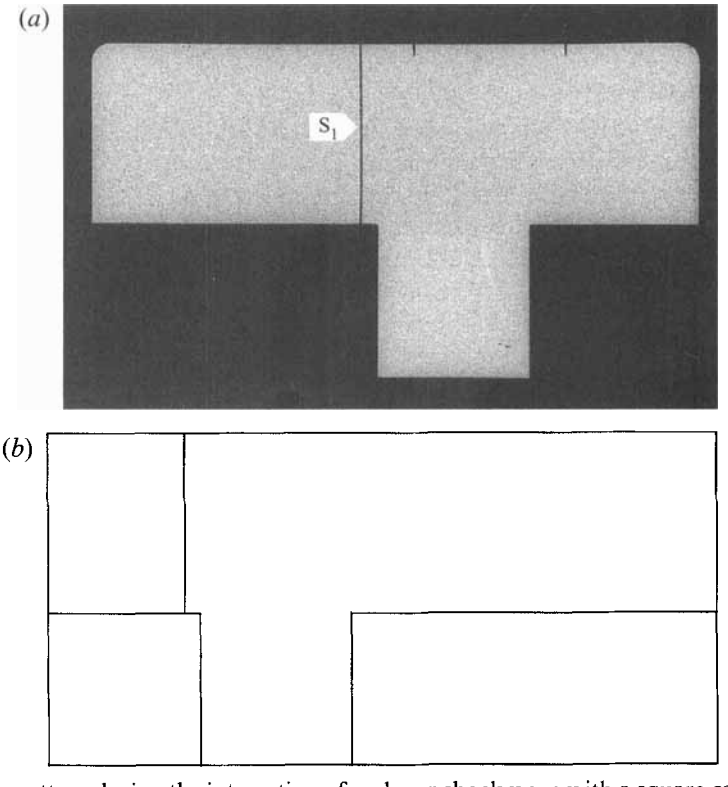

FIGURE 3. Wave pattern during the interaction of a planar shock wave with a square cavity. $t = 0$ μs. (*a*) Shadowgraph, (*b*) numerical simulation (990 × 495 equal-size grid). Initial conditions are: $M_s = 1.30$, $P_0 = 0.97$ bar and $T_0 = 23.3$ °C.

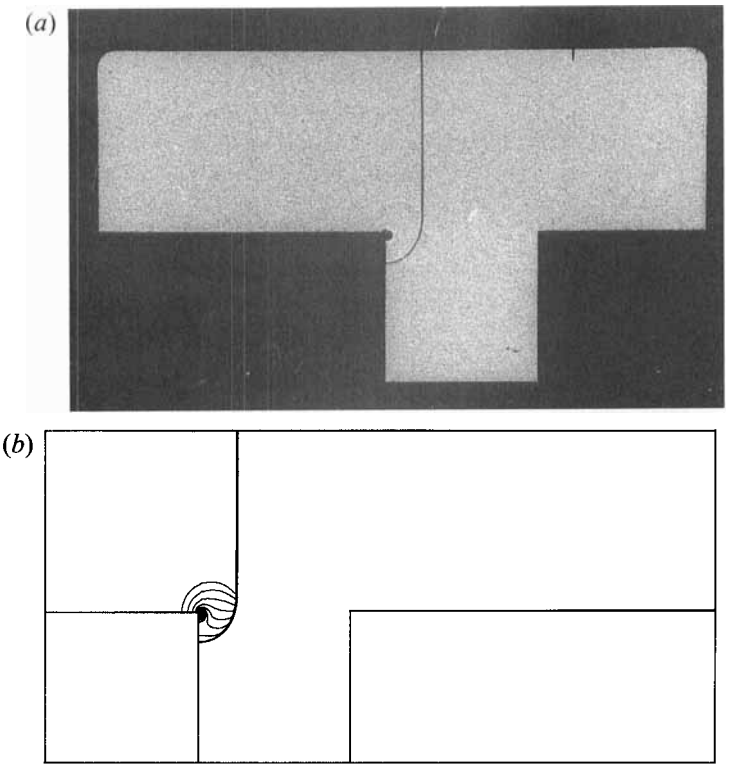

FIGURE 4. As in figure 3 but at $t = 40$ μs.

at the centre of the three surfaces composing the square cavity, see figure 1. The pressure measurements were made for incident shock wave Mach numbers within the range $1.15 \leqslant M_s \leqslant 2.17$.

As mentioned above, for the case where $M_s = 1.30$ shadowgraphs were taken every 20 μs resulting in 22 photographs covering the entire interaction time. In order not to overwhelm the presentation, only some of the photographs are shown below. All shadowgraphs are labelled (*a*) while the corresponding numerical simulations are marked (*b*). The incident shock wave, $M_s = 1.30$, propagates into a quiescent air at $T_0 = 23.3$ °C and $P_0 = 0.97$ bar. The sequence of figures 3(*a*) to 13(*a*) shows the evolution of the various waves which resulted from the interaction of the incident shock wave S_1 with the square cavity. In the shadowgraph shown in figure 3(*a*) the incident shock wave S_1 is shown a short time before it reaches the cavity's leading edge. In the shadowgraph shown in figure 4(*a*), taken 40 μs later, the first stage of the interaction process is shown; S_1 starts diffracting around the cavity's upper-left corner, shedding a vortex behind it. The numerical simulation, shown in figure 4(*b*), reconstructs the shadowgraph of figure 4(*a*) precisely. The lines appearing in figure 4(*b*), as well as in part (*b*) of all the following figures, are lines of constant density. The distance traversed by the incident shock wave S_1, relative to its position 40 μs earlier and the magnitude of its descent down the cavity are the same in figures 4(*a*) and 4(*b*). With increasing time S_1 propagates toward the cavity's exit and toward its bottom, while the vortex grows in size and remains close to the cavity's upper-left corner, e.g. see figure 5(*a*) which was taken 60 μs after the shadowgraph shown in figure 4(*a*). Again, perfect agreement regarding the shock wave and the vortex geometry and location exist

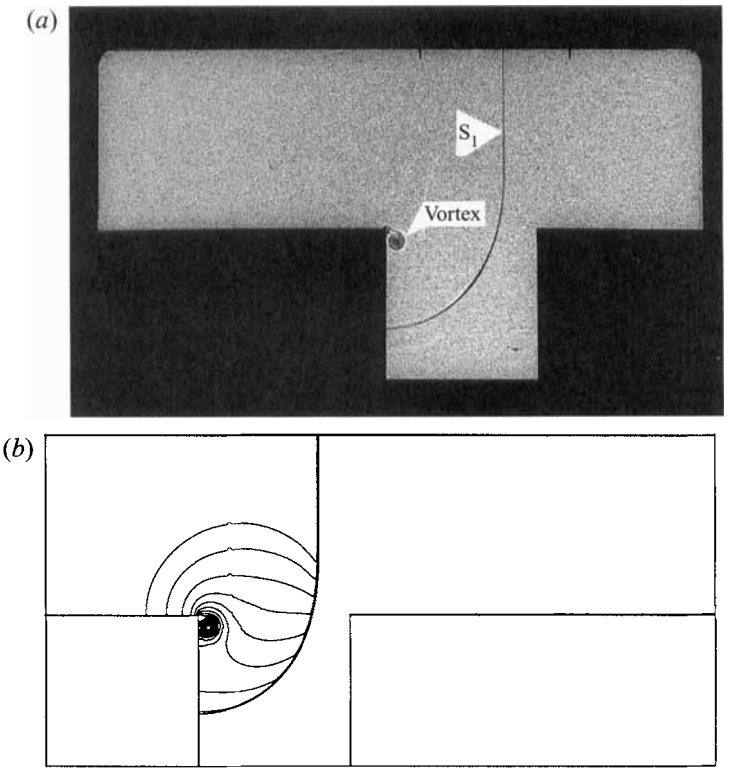

FIGURE 5. As in figure 3 but at $t = 100$ μs.

between the experimental (figure 5*a*) and the numerical (figure 5*b*) results. This process continues until S_1 hits the cavity upper-right corner, as shown in figure 6(*a*), which was taken 40 μs after figure 5(*a*). Now S_1 splits into a transmitted (S_1) and a reflected (Sr_1) shock waves. Since the cavity has equal-length walls, it is obvious from figure 6(*a*) that the part of the incident shock wave S_1 which propagates along the shock tube axis is faster than the part which descends toward the cavity's bottom. During the process shown in the shadowgraphs of figures 4(*a*) to 6(*b*), the vortex grows in size and its centre slowly moves away from the cavity's upper-left corner.

It should be noted that although every real fluid is viscid, and our theoretical model assumes an inviscid fluid, the numerical simulations exhibit a corner-shed vortex akin to the one observed in the experiment. The 'inviscid' mechanism by which this vortex is generated is the strongly rotational flow generated by the curved shock wave resulting from the expansive diffraction of the incident shock wave over the upper-left corner of the cavity. Apparently, at early times this mechanism is the dominant one and lack of viscosity does not significantly alter the vortex formation. Note however, that this argument is valid with respect to an analytic solution to the Euler equations describing the corner shock diffraction. In the numerical solution, truncation errors invariably give rise to a 'numerical viscosity', so that strictly speaking, the numerical solution is never perfectly inviscid. Just the same, no wall friction is present, so that with respect to the vortex shedding process, vorticity is generated by the 'inviscid mechanism' previously described, and the wall boundary layer is absent. When inspecting the vortices in figures 7(*a*) and 7(*b*) the lack of the slipstream connecting the vortex to the corner is apparent in the numerical simulations. This may be attributed to numerical advection errors which invariably smear out sharp density variations. The

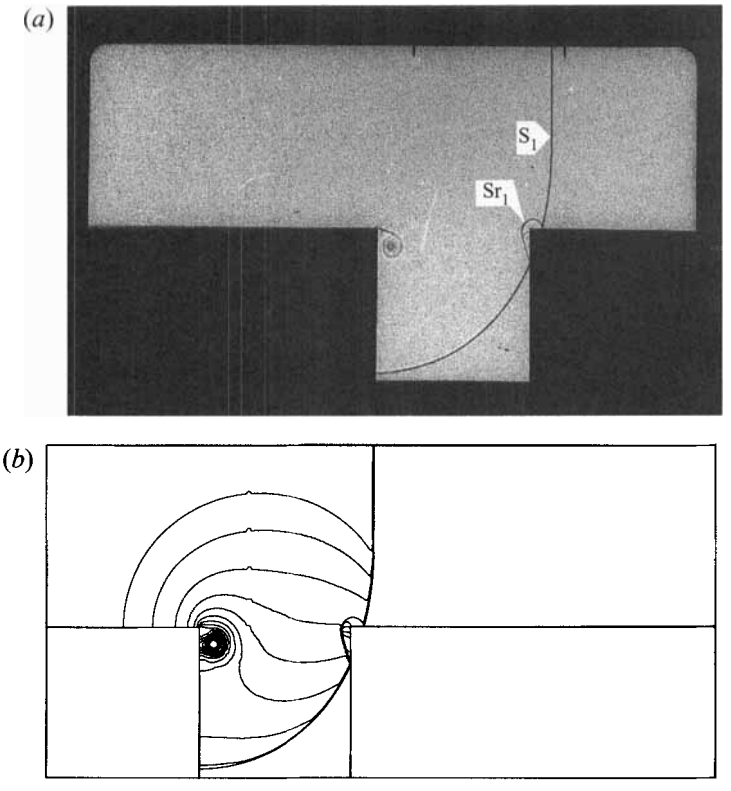

FIGURE 6. As in figure 3 but at $t = 140$ μs.

existence of a slipstream in the simulation is better detected by referring to the velocity plots (figure 15*c*, *d*). Clearly, the horizontal velocity component is continuous around the corner, while the vertical component along the cavity left-hand wall seems to approach zero near the corner. Please note that in figure 15(*c*, *d*), the velocity vectors are reduced by a ratio of 1:15, i.e. every plotted velocity vector represents the value at the mid-cell in a cluster of 15 × 15 cells. If we were to examine the detailed velocity map, the magnitude of the vertical component in the cell just below the corner would be much smaller than indicated on the plot. To summarize this discussion, the slipstream, although poorly represented by the isopycnic plot, is better shown in the velocity plot.

In the shadowgraph shown in figure 7(*a*), taken 20 μs after that shown in figure 6(*a*), the descending part of S_1 has reached the cavity's bottom and is reflected upward as Sr_2. S_1' is the part of S_1 which is still moving toward the cavity's lower-right corner. The reflected shock wave Sr_1 and a second reflected wave Sr_4 are also visible in figure 7(*a*). All these waves are clearly reproduced in the numerical results shown in figure 7(*b*). Again, perfect agreement exists between the two findings. As time progresses (figure 8*a*), S_1' approaches the cavity's lower-right corner and therefore its size decreases while Sr_2 and Sr_1 become larger and weaker (on a shadowgraph, the stronger the shock wave is, the darker it appears in the photograph). Sr_4 also increases in size and becomes much weaker; it is hardly noticeable in figure 8(*a*). In the numerical results weak waves are shown by thin lines while strong waves appear as thick lines. It is clear from figure 7(*b*) that the upper part of Sr_1 is weaker than its lower part. The weak wave Sr_4 in figure 8(*a*) is too weak to be noticed in figure 8(*b*). However, all other waves shown in figure 8(*a*) are correctly reproduced in the numerical results shown in figure 8(*b*). A unique

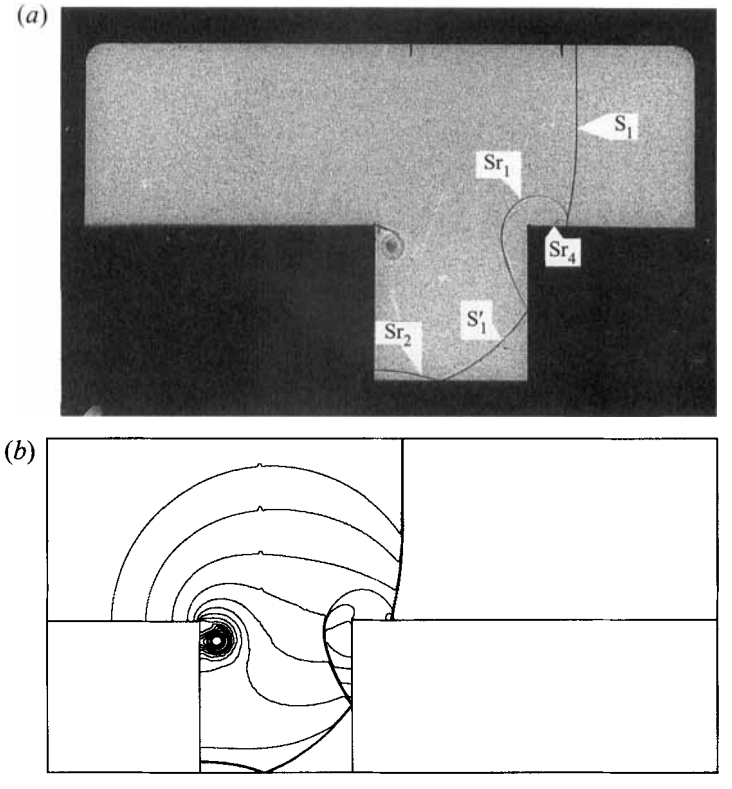

FIGURE 7. As in figure 3 but at $t = 160$ μs.

situation exists in the shadowgraph of figure 9(*a*); it was taken at the exact moment when S_1' hits the cavity's lower-right corner, displaying a meeting between Sr_1 and Sr_2 at this corner. This happens 200 μs after the situation shown in figure 3(*a*). The numerical results shown in figure 9(*b*) reconstruct this unique wave pattern accurately. In the present case Sr_1 grows in size and its first part, that starting from S_1 immediately behind the end of the Mach stem, gets still weaker. Sr_4 is reduced to a Mach wave and is therefore unrecognizable on figure 9(*a*). The vortex continues its movement away from the cavity upper-left corner. In figure 9(*b*) the upper part of Sr_1 is too weak to be noticed. As mentioned above, all numerical reconstructions show lines of constant density. In the present solution the density change between neighbouring lines of constant density is set at $\Delta\rho/\rho_0 = 0.054$. The choice of $\Delta\rho/\rho_0$ controls the density resolution of the numerically constructed flow field. Inspecting the sequence of figures 8, 9, 10 we note that at the lower-right corner of the cavity the remainder of the incident shock wave S_1' has vanished (figure 9) upon reaching the corner, and has re-emerged as the reflected shock wave S_{r1}' (figure 10). Note the good agreement of the computational simulations in this sequence with the corresponding experimental shadowgraphs.

So far the wave pattern has been controlled mainly by the interaction of S_1 with the three walls of the square cavity. At the time of figure 10, three shock waves are present within the cavity and their continued interactions with each other, with the cavity walls and with the vortex, are exhibited in the following shadowgraphs. Such multiple interactions lead to many reflections and distortions of the participating waves. The beginning of the complex collision/reflection process which takes place inside the

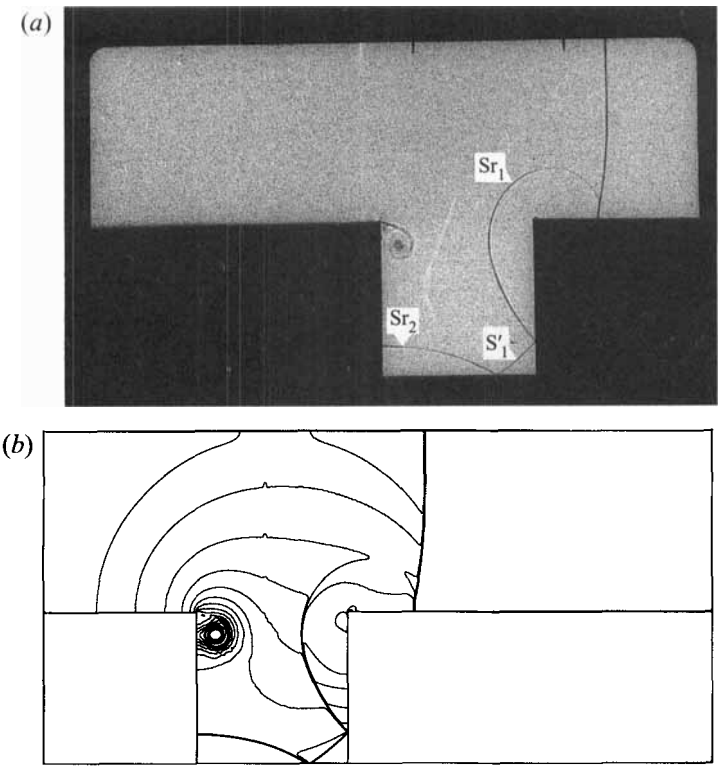

FIGURE 8. As in figure 3 but at $t = 180$ μs.

cavity is shown in figure 11(*a*) which was taken 40 μs after figure 10(*a*). The wave geometry is almost identical in both figures 11(*a*) and 11(*b*) indicating both the accuracy of the present numerical solution and the validity of the physical model proposed for the interaction considered, (1)–(4). With passing time the flow and wave configuration inside the cavity become more and more complex as can be seen from the shadowgraph shown in figure 12(*a*), which was taken 60 μs after that of figure 11(*a*). All the relatively strong waves which appear in figure 12(*a*) are also shown correctly in figure 12(*b*). Note that the curvature and the geometrical location of these waves are very well reproduced in the numerical simulation. The waves and the vortex centre position, relative to the cavity's walls/corners, are reproduced with high accuracy. In the shadowgraph shown in figure 13(*a*), taken 80 μs after that in figure 12(*a*), a large web of waves of various strengths is shown. The wave pattern is a result of multiple interactions among the waves and between the waves and the cavity's walls, and also between waves and the vortex. The geometry and position of the strong waves and the vortex centre are well reproduced in the numerical solution shown in figure 13(*b*). Reducing the value of $\Delta\rho/\rho_0$ from the chosen value of $\Delta\rho/\rho_0 = 0.0540$ and/or increasing the number of grid points would have helped in revealing the weaker waves discernible in figure 13(*a*) but not observed in figure 13(*b*).

The effect of an increase in the number of grid points used for the numerical solution becomes apparent when the results shown in figure 7(*b*) (the wave configuration 160 μs after the situation shown in figure 3*b*) are re-calculated using a smaller number of grid points. The results shown in figure 14 were obtained for a mesh of 660×330, instead of the 990×495 used for obtaining figures 3(*b*)–13(*b*). It is clearly seen that figure 7(*b*) reproduces figure 7(*a*) more accurately than figure 14, where the reflected wave Sr_2

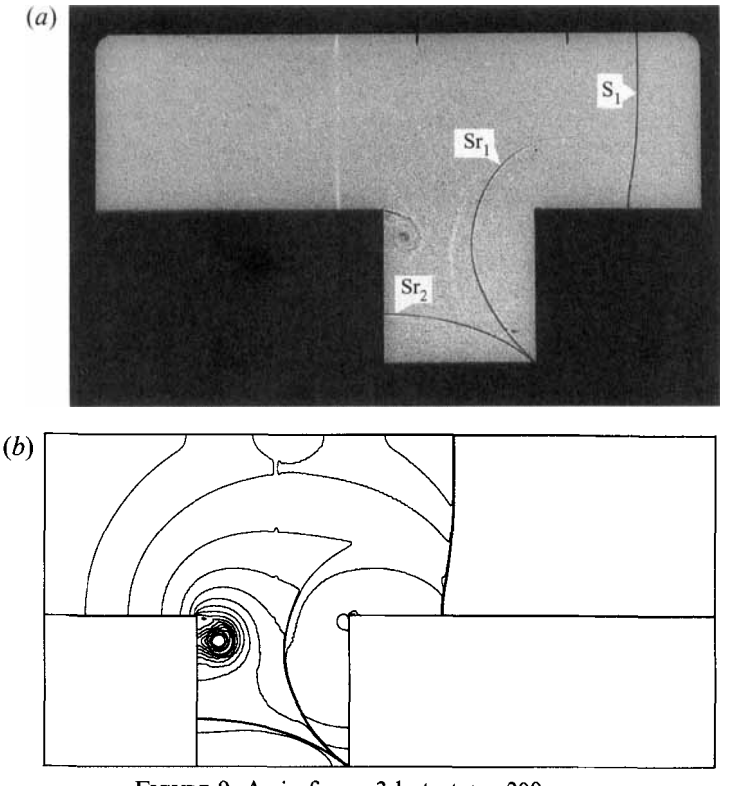

FIGURE 9. As in figure 3 but at $t = 200$ μs.

appears as a weak shock wave (two lines) while it appears as a well defined reflected wave in figure 7(*b*). Sr_4 appears as a weak wave in figure 7(*b*), but does not appear in figure 14. Also, while in figure 7(*b*) Sr_1 has the exact geometry shown in the shadowgraph of figure 7(*a*) it is not reproduced accurately in figure 14. Owing to memory limitations of the computer used (IBM RS 6000/560) a solution with a finer grid was not attempted. Obtaining the present results (990×495 grid) required 40 hours for the given incident shock wave Mach number.

In the present case ($M_s = 1.30$) the flow behind the incident shock wave is subsonic, which is why a vortex is generated at the cavity's upper-left corner, where the post-shock flow experiences expansion. This vortex remains attached to the corner through a slipstream, see figures 4(*a*) to 11(*a*). The slipstream is eventually destroyed by the colliding shock waves inside the cavity, see figures 12(*a*) and 13(*a*). The numerical solution provides information on all the flow variables: for example the flow velocity map, at a few different times, as shown in figure 15(*a–d*). In figure 15(*a*) the flow velocity is shown for $t = 0$, the situation shown in figure 3. As could be expected, the flow behind the incident shock wave is uniform and parallel to the shock tube walls. Upstream of the incident shock wave the entire field is quiescent, i.e. $u = 0$. The velocity field corresponding to figure 5 is shown in figure 15(*b*); the existence of a vortex close to the cavity's upper-left corner is represented by rapid changes in the direction and magnitude of velocity vectors at that region. Ahead of the incident shock wave the gas is at rest. The velocity field corresponding to figure 8 is shown in figure 15(*c*). The flow expansion around the vortex and behind the various waves is clearly shown. As could be expected, there is zero velocity behind the stopping shock Sr_2. The velocity field at the time that the shadowgraph of figure 12(*a*) was taken is shown in

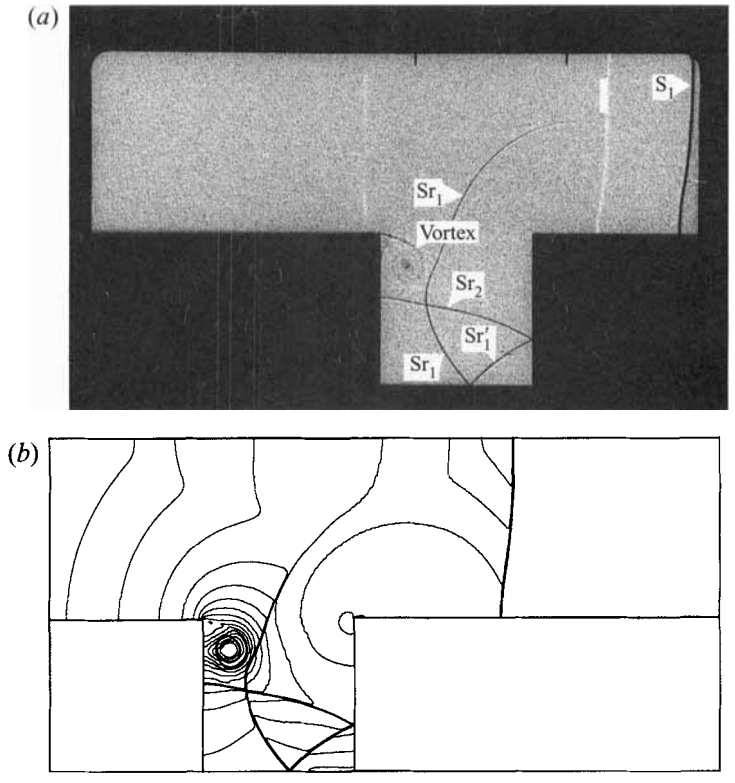

FIGURE 10. As in figure 3 but at $t = 240$ μs.

figure 15(*d*). It is clear from this figure that in spite of the shock collision with the vortex, the later is still well defined and remains quite close to the cavity's upper-left corner. Velocities close to most of the cavity's walls at the time considered are very small, as should be expected behind wall-reflected shock waves.

A different wave pattern and flow behaviour are observed when the incident shock wave Mach number is raised to a level that results in a supersonic flow behind it. Such a case is obtained for example when $M_s = 2.032$. The results shown in figures 16 to 22 were obtained experimentally (shadowgraphs are marked *a*) and numerically (*b*) for a case when the above mentioned incident shock wave propagates into a quiescent air at $T_0 = 22.6$ °C and $P_0 = 0.9$ bar. In the experimental work the incident shock wave Mach number was deduced by measuring the time that elapsed between the shock's arrival at two pressure transducers, each placed at a different point on the shock tube wall. From the known distance between these pressure transducers and the measured time of arrival, the incident shock wave velocity is readily deduced. The shock wave Mach number is based on this velocity and the measured pre-shock gas temperature. For the set of results shown in figures 16(*a*) to 22(*a*), the measured incident shock wave Mach number was 2.085. The very good agreement that was obtained between the experimental results (shadowgraphs) and the numerical simulations, was achieved when M_s was taken as $M_s = 2.032$; this is 2.5% lower than the measured value. The difference is due to experimental errors and to shock wave attenuation between the place of measurement and the shock tube test section where the shadowgraphs were taken. Note that the shock wave velocity deduced from the wave position in the shadowgraphs agrees perfectly with $M_s = 2.032$.

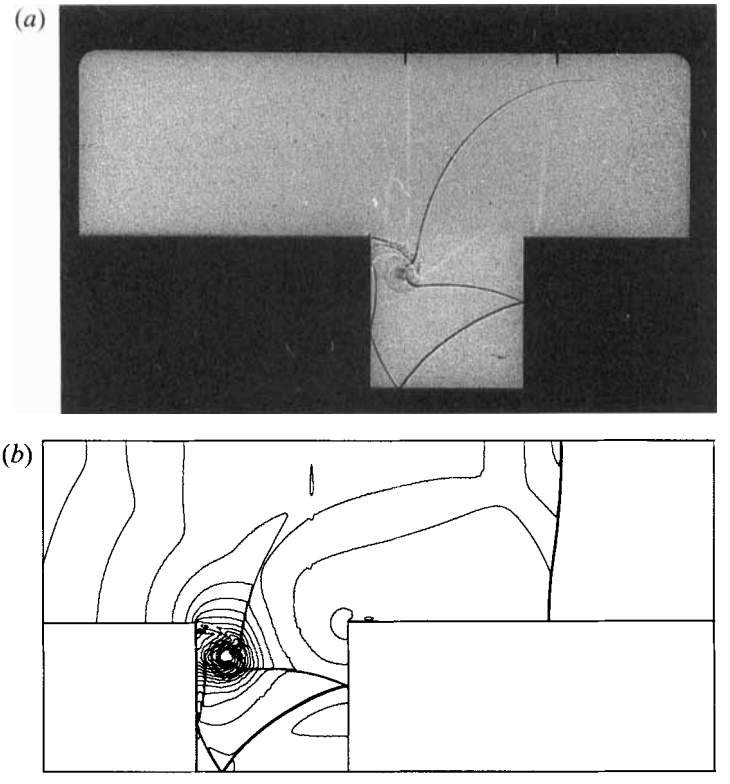

FIGURE 11. As in figure 3 but at $t = 280$ μs.

As before, in the numerical solution the flow field was divided into a grid of 990×495. Since now the incident shock wave is much stronger than that in the previous case, the density jump between neighbouring lines of constant density (shown in figures 17*b* to 22*b*) is increased to $\Delta\rho/\rho_0 = 0.1179$.

In figure 16(*a*) the incident shock wave is shown shortly before it hits the cavity's leading edge; as could be expected, figure 16(*b*) replicates the shadowgraph shown in figure 16(*a*). The shadowgraph shown in figure 17(*a*) was taken 37.5 μs after that of figure 16(*a*). The diffraction of the incident shock wave over the cavity's upper left corner is shown clearly in figures 17(*a*) and 17(*b*). Unlike the previously described case, now the post-shock flow velocity is almost sonic. Since the post-shock flow is sonic, instead of a vortex near the cavity's upper-left corner (which characterized the flow expansion in the previously described case), we now have an expansion wave centred at the corner. This expansion wave is shown very clearly in figure 17(*b*), but is hardly noticed in figure 17(*a*) because shadowgraphs are sensitive to changes in density gradients. Large changes in density gradients are present at shock fronts, therefore S_1 and S_2 are clearly visible in figure 17(*a*). Such gradient changes are understandably small in regions of the expansion wave that are not very close to the corner, and therefore are not observed on the shadowgraph. However, the entire centred expansion wave is clearly visible in the numerical simulation (figure 17*b*). As could be expected, since the flow behind the incident shock (S_1) is almost sonic, the initial slope (near the wall) of the expansion wave head is vertical to the flow direction (see figure 17*b*). The density changes which occur in the expansion are clearly visible in the numerical simulation where the centred fan pattern (akin to a self-similar Prandtl–Meyer flow) is

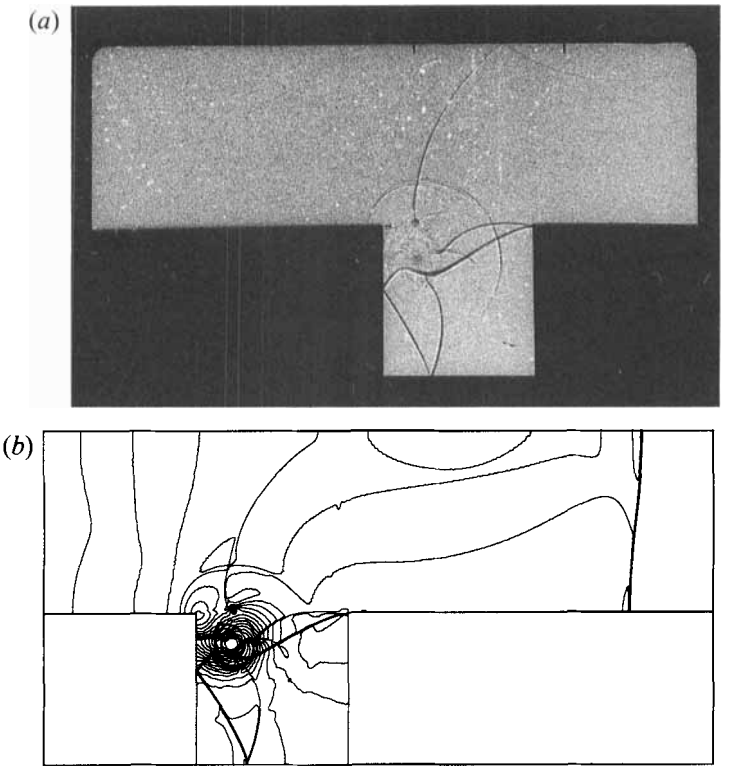

FIGURE 12. As in figure 3 but at $t = 340$ μs.

readily noticed. In order to match between the high-pressure zone which exists behind S_1 and the low pressure behind the expansion wave centred at the cavity's upper left corner, a secondary, upstream-facing, shock wave (S_2) is generated. This shock wave, is clearly visible in the shadowgraph (figure 17*a*) and in the numerical simulation (figure 17*b*). It should be noted that both the shock wave position and its geometry are reproduced accurately in the numerical solution shown in figure 17(*b*).

The shadowgraph shown in figure 18(*a*), taken 37.5 μs after that of figure 17(*a*), clearly shows that the unperturbed part of S_1 propagates faster than the part descending into the cavity. This was also observed in the previously discussed case of the weaker incident shock ($M_s = 1.30$). The numerical simulation shown in figure 18(*b*) matches the shadowgraph perfectly. In both, the 'S'-shaped upstream-facing shock wave S_2 has the same shape, size and position. The same is true for S_1. The slipline C_1 separating the flow fields generated behind shock waves S_1 and S_2 is clearly seen both in the shadowgraph and in the numerical simulation. The fact that C_1 is a slipline can be confirmed by inspecting figure 18(*c*) which shows lines of constant pressure (isobars). As could be expected, shock waves S_1 and S_2 are clearly visible in figure 18(*c*), while C_1 is absent, since equal pressures exist on both sides of a slipline. 25 μs later, the reflection of the incident shock wave S_1 from the cavity's right-hand wall and its interaction with the cavity's upper-right corner is clearly visible; see figure 19(*a*). It is apparent from this shadowgraph that the part of S_1 which descends into the cavity is weaker than the part which propagates along the shock tube axis (it appears brighter than the part of S_1 which propagates along the tube's axis). This fact can also be deduced from its slower movement; it had not reached the cavity's bottom while the

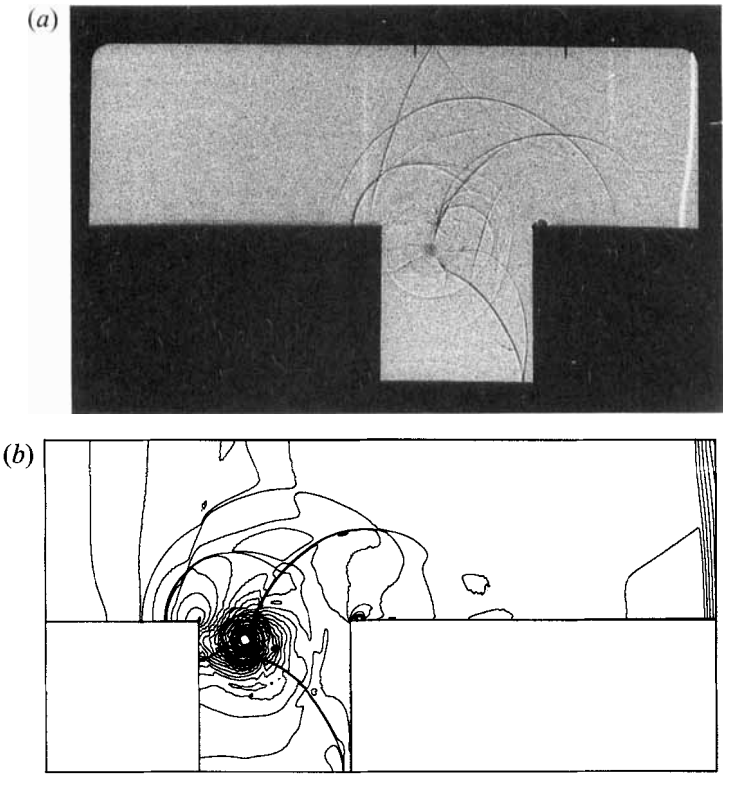

FIGURE 13. As in figure 3 but at $t = 420$ μs.

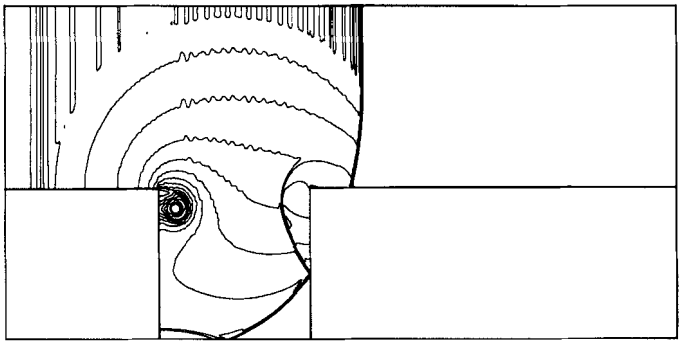

FIGURE 14. Numerical simulation, using a 660×330 equal-size grid, of the wave pattern during interaction of a planar shock wave with a square cavity; $t = 160$ μs.

part moving along the tube's axis has traversed a longer distance. Sr_1 and S_2 appear as strong shock waves while C_2, a slipline starting from the triple-point, is barely noticeable. All these waves are accurately reproduced numerically in figure 19(*b*). The shadowgraph shown in figure 20(*a*) describes the situation 25 μs later. Now two reflected shock waves are clearly shown; Sr_1 which was reflected from the cavity's right wall and Sr_2 which was reflected from the cavity's floor. S_1' is the part of S_1 which has not yet reached the cavity's walls; it propagates toward the cavity's lower-right corner. S_2 is also clearly visible in figure 20(*a*); through this shock wave, the pressure matching between the low-pressure zone arising from the corner expansion wave and the high-

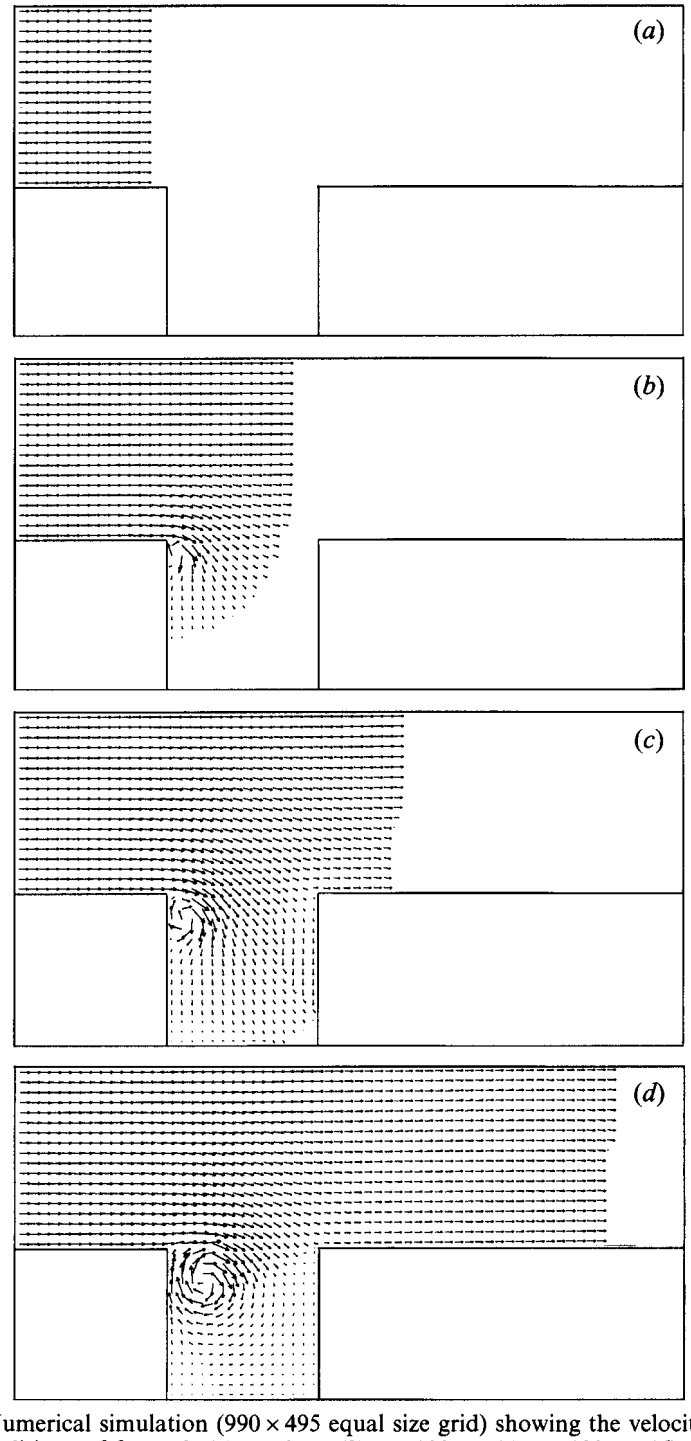

FIGURE 15. Numerical simulation (990 × 495 equal size grid) showing the velocity field for the initial conditions of figure 3. (*a*) $t = 0$ μs, (*b*) $t = 100$ μs, (*c*) $t = 180$ μs, (*d*) $t = 340$ μs.

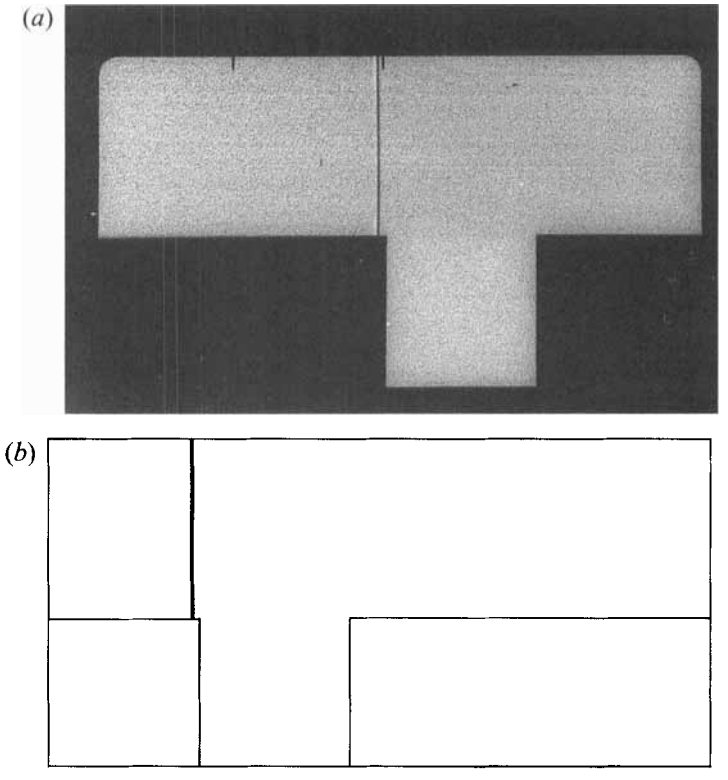

FIGURE 16. Wave pattern during the interaction of a planar shock wave with a square cavity. $t = 0$ μs. (*a*) Shadowgraph, (*b*) numerical simulation (990 × 495 equal-size grid). Initial conditions are: $M_s = 2.032$, $P_0 = 0.90$ bar and $T_0 = 22.6$ °C.

pressure zone that exists behind Sr_1 takes place. Therefore, S_2 extends throughout the low-pressure zone downstream of the corner. Weaker flow discontinuities are also visible in this shadowgraph (figure 20*a*), for example, slipline C_1 and slipline C_2 which starts from the triple point. Figure 20(*c*), in which isobars are presented, confirms that C_1 and C_2 are sliplines. All these shock waves and other flow discontinuities are reproduced very accurately, in shape and location, in the numerical reconstruction shown in figure 20(*b*). The wave pattern which exists 25 μs later is shown in the shadowgraph of figure 21(*a*) and the appropriate numerical simulation is shown in figure 21(*b*). The incident shock wave S_1 has almost left the optical field of view; S_2 approaches Sr_1 and still extends throughout the low-pressure zone across the corner expansion wave, as could be expected. The reflected shock waves, Sr_1 and Sr_2, intersect each other resulting in a complex Mach reflection near the cavity's lower-right corner. Additional, weaker, flow discontinuities are detectable in the shadowgraph, and in the numerical simulation, such as sliplines C_1 and C_2. As before, excellent agreement on the waves geometry and location exists between experimental and numerical results. It should be noted that since the flow behind the incident shock wave, S_1, is almost sonic (for $M_s = 2.032$ the post-shock flow Mach number is 0.98), the first characteristic of the expansion wave moves slightly upstream of the cavity's upper-left corner; see figure 21(*b*). With increasing time this minute advance, upstream of the expansion corner, continues. The initial slope of this characteristic, as could be expected, is vertical relative to the flow direction. With increasing time, S_2 will collide with Sr_1 and with other waves present inside the cavity; in addition to these mutual interactions, these

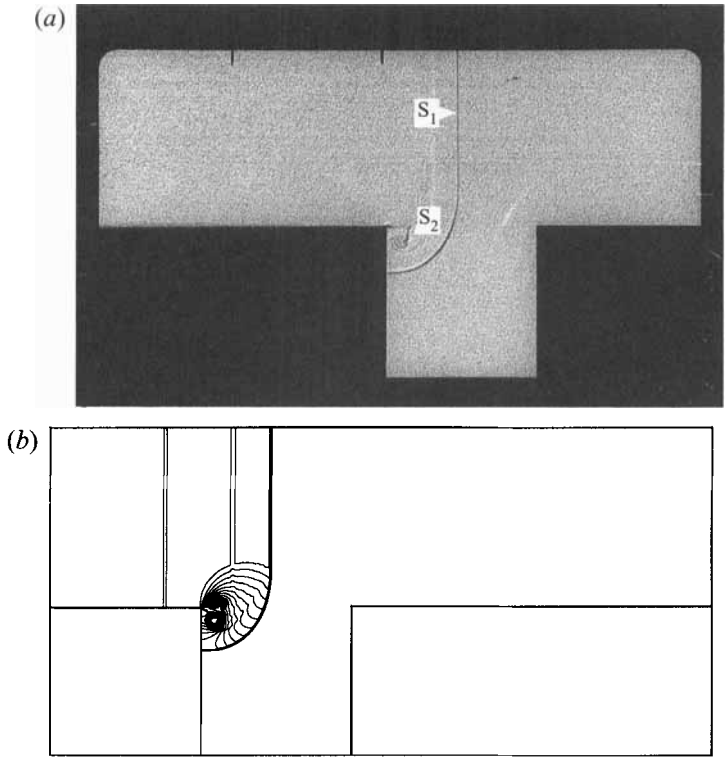

FIGURE 17. As in figure 16 but at $t = 37.5$ μs.

waves will collide with the cavity's walls resulting in a very complex flow. Some idea of this complex flow is given in figure 22 which shows the wave pattern 100 μs after that shown in figure 21. Again, as could be expected, excellent agreement exists between experimental (figure 22*a*) and numerical (figure 22*b*) results. At this late time many shock waves and contact discontinuities are present inside the cavity; they are the result of the multiple interactions mentioned earlier. At an earlier time (figures 17 to 21) a clear corner expansion wave is observed in all numerical simulations. At a late time the complex wave pattern prevailing inside the cavity (figure 22*b*) interferes with the centred expansion wave and as a result the expansion wave is divided into a few segments, each terminated by a shock wave. Owing to the high density gradients present in the case considered ($M_s = 2.032$), most of the shock waves and other discontinuities appear much clearer in the numerical simulations than in the shadowgraphs. This was not the case for the weaker shock wave ($M_s = 1.30$) discussed earlier.

In figure 23 a comparison between experimentally obtained and numerically evaluated pressure-history peaks is given. Three pressure pickups (figure 1) were programmed to record the peak in the pressure time-history. The experimental findings were obtained using Kistler 606 piezoelectric pressure transducers, they are presented in figure 23 as discrete points; the numerical results are shown as solid lines. All pressures were normalized by the pre-shock pressure, P_0. As could be expected, for a given shock wave pressure ratio (P_2/P_0) the highest pressures are encountered on the cavity wall facing the incident shock wave (where pressure gauge no. 3, shown in figure 1, is located). The lowest pressures are experienced by the wall along which the incident shock wave diffraction takes place (where pressure gauge no. 1 is located). This is in

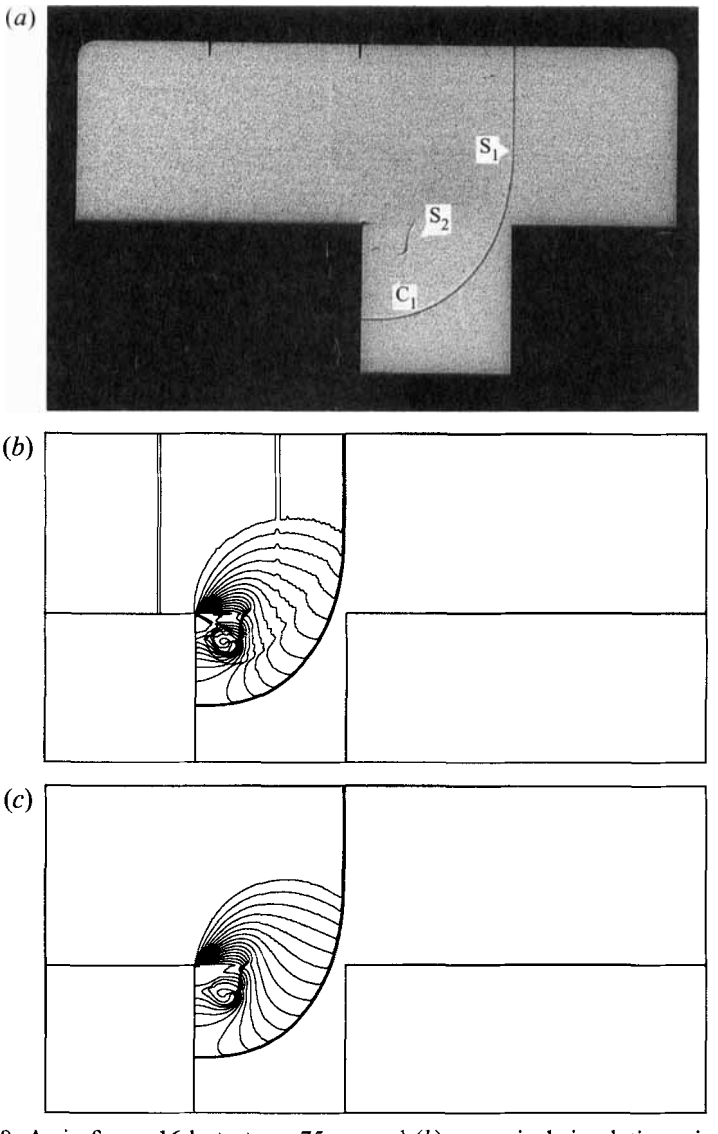

FIGURE 18. As in figure 16 but at $t = 75$ μs, and (*b*) numerical simulation – isopicnics, (*c*) numerical simulation – isobars.

line with the fact mentioned previously, while discussing the shadowgraphs in which the incident shock wave diffraction is shown, that the diffracting part of the incident shock wave is weaker (slow propagation) than the transmitted part. Increasing the strength of the incident shock wave (i.e. increasing P_2/P_0) results in an increase in pressures acting on all the cavity walls. It is evident from figure 23 that a very good agreement exists between the experimental and numerically calculated pressures. A further confirmation of the validity and accuracy of the proposed physical model (equations (1)–(5)) and its numerical solution (the GRP scheme) is provided by this agreement.

In Gvozdeva *et al.* (1988) and Bazhenova *et al.* (1990) the prevailing wave pattern was recorded at some 'frozen' times. There is no information in those papers about the time evolution of the flow considered. As is obvious from figures 3 to 22, time plays

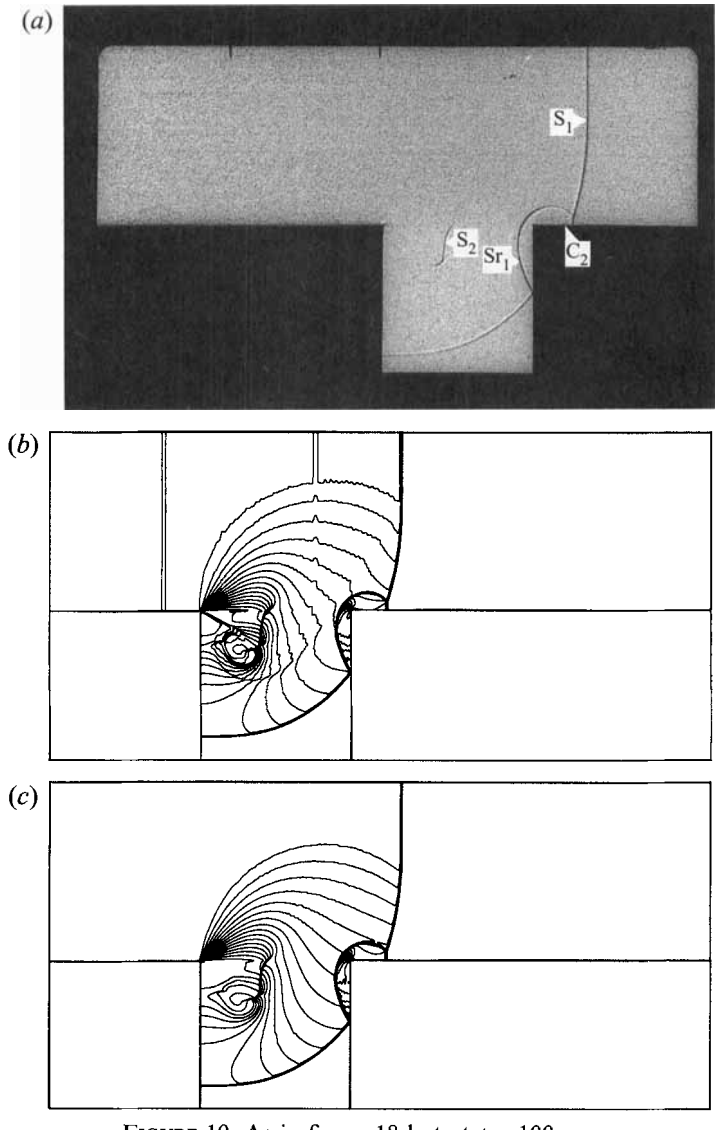

FIGURE 19. As in figure 18 but at $t = 100$ μs.

a major role in this interaction process. Furthermore, their predictions regarding peak pressures inside the cavity are far from reality.

5. Summary and conclusions

The flow resulting from the interaction between a planar shock wave and a square cavity was studied in detail, both experimentally and numerically. It was shown that the complex time-dependent flow could be computed accurately using the second-order GRP scheme. An excellent agreement regarding the prevailing shock fronts location and geometry was found between experimental (shadowgraphs) and numerical results. It was shown that the flow which started as a self-similar one turned quickly into a genuinely time-dependent flow in which no self-similarity existed. As could be expected, the highest peak pressures are experienced by the cavity wall on which a

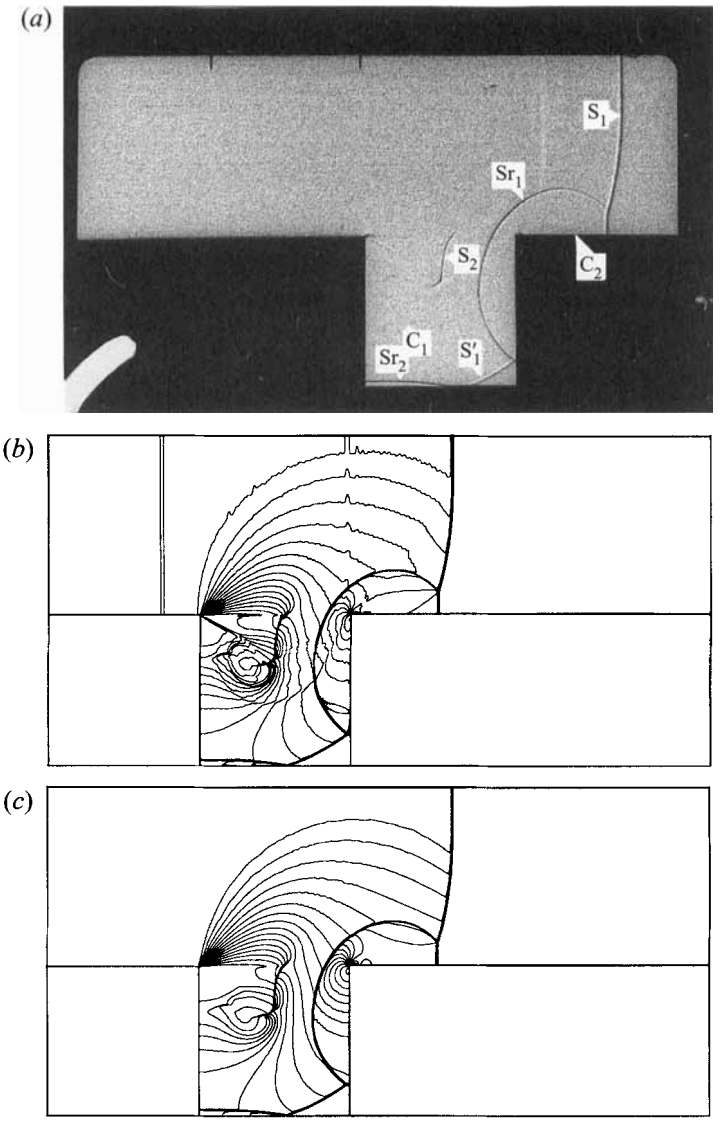

FIGURE 20. Wave pattern during the interaction of a planar shock wave with a square cavity. As in figure 18 but at $t = 125$ μs.

head-on collision with the incident shock wave takes place. The lowest peak pressures are found on the cavity wall along which the incident shock wave diffraction takes place. The flow developed inside and around the cavity depended on the strength of the incident shock wave. In air, for $M_s < 2$ the post shock flow is subsonic and the flow expansion into the cavity is via a vortex. For $M_s > 2$ the post-shock flow is supersonic and the flow expansion into the cavity is through a centred expansion wave. The interactions between the various waves reflected from the cavity walls, and between them and the vortex or the centred expansion wave, produced a complex unsteady flow in which no self-similar structure could be observed. In spite of the complexity of such flows, they are governed by a fairly simple physical model, equations (1)–(5) (Euler equations), and can be solved numerically (using the GRP scheme) yielding very accurate results. It is concluded that the present physical model and its numerical

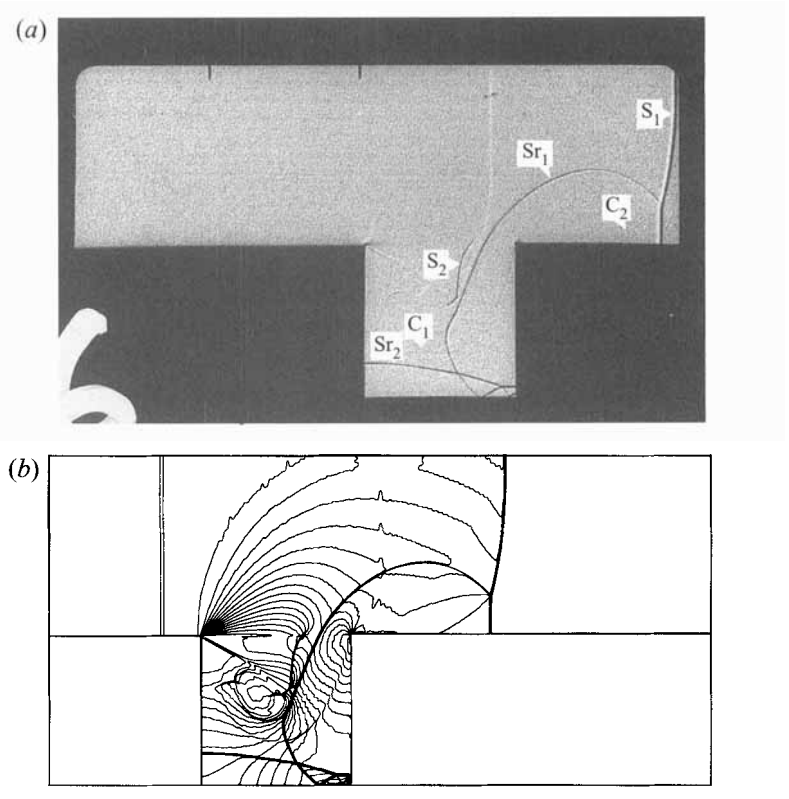

FIGURE 21. Wave pattern during the interaction of a planar shock wave with a square cavity. As in figure 16 but at $t = 150$ μs.

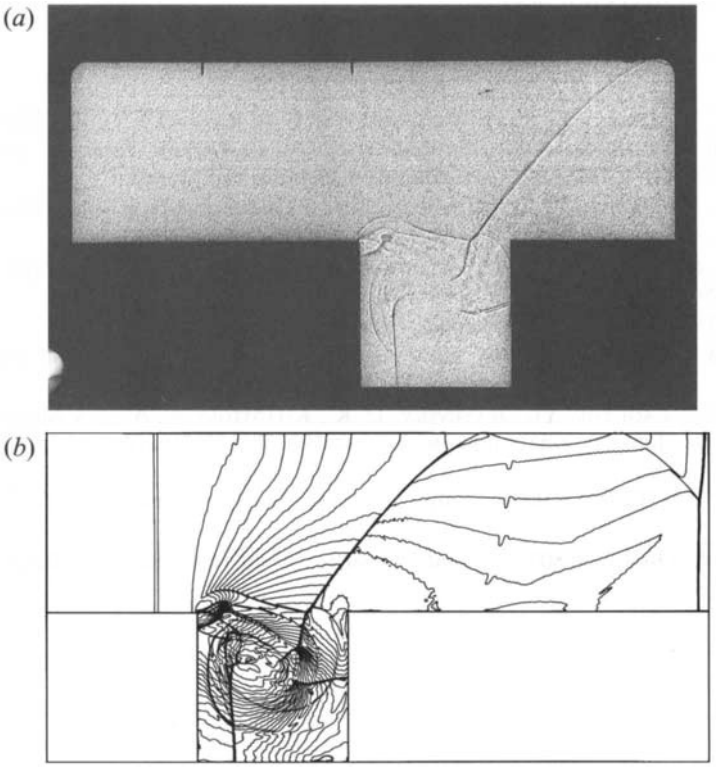

FIGURE 22. As in figure 16 but at $t = 250$ μs.

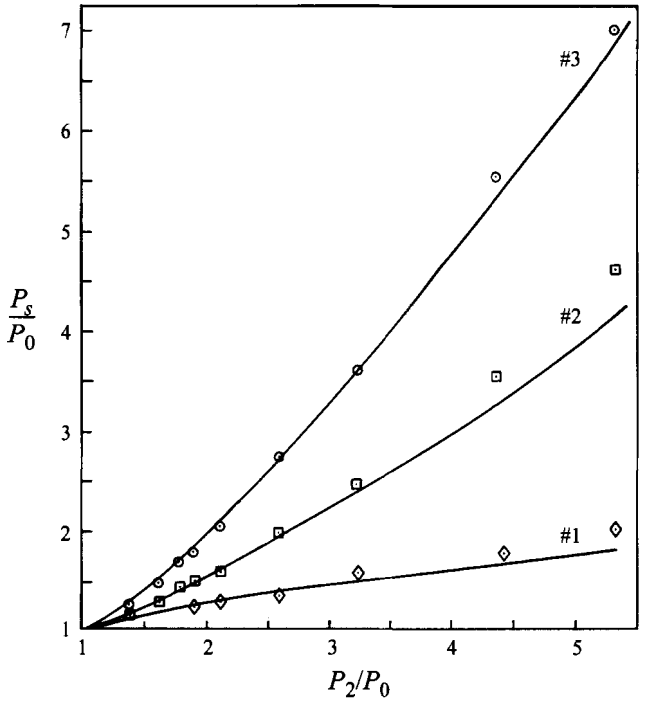

FIGURE 23. First pressure peaks on each of the cavity walls: ◇, gauge, no. 1; ⊡, gauge no. 2; ⊙, gauge no. 3; ——, numerical results.

solution can be used reliably for treating other two-dimensional compressible flows where real gas effects are negligible.

REFERENCES

BAZHENOVA, T. V., GVOZDEVA, L. G., LAGUTOV, YU. P. & RAYEVSKY, D. K. 1990 Nonstationary interaction of a shock wave with shallow cavity. In *Current Topics in Shock Waves* (ed. Y. W. Kim). AIP Conf. Proc. 208. American Institute of Physics.

BEN-ARTZI, M. & FALCOVITZ, J. 1984 A second-order Godunov-type scheme for compressible fluid dynamics. *J. Comput. Phys.* **55**, 1–32.

BEN-ARTZI, M. & FALCOVITZ, J. 1986 An upwind second-order scheme for compressible duct flows. *SIAM J. Sci. Statist. Comput.* **7**, 744–768.

BEN-DOR, G. 1991 *Shock Wave Reflection Phenomena.* Springer.

FALCOVITZ, J. & BEN-ARTZI, M. 1995 Recent developments of the GRP method. *JSME Intl J.* B **38**, 497–517.

GVOZDEVA, L. G., LAGUTOV, YU., RAYEVSKY, D. K., KHARITOVNOV, A. E. & SHAROV, YU. L. 1988 Investigation of nonstationary flows with separation over cavities. *Izv. Mekh. Zidk. Gaza* No. 3, 185–191.

LEER, B. VAN 1979 Towards the ultimate conservative difference scheme V. *J. Comput. Phys.* **32**, 101–136.

STRANG, G. 1968 On the construction and comparison of difference schemes. *SIAM J. Numer. Anal.* **5**, 506–517.